PHYSICAL REVIEW E **73**, 016405 (2006)

Quasimonoenergetic electron beam generation by using a pinholelike collimator in a self-modulated laser wakefield acceleration

N. Hafz, M. S. Hur, and G. H. Kim
Center for Advanced Accelerators, Korea Electrotechnology Research Institute, Changwon 641-120, Korea

C. Kim and I. S. Ko
Pohang Accelerator Laboratory, Pohang 790-784, Korea

H. Suk
Center for Advanced Accelerators, Korea Electrotechnology Research Institute, Changwon 641-120, Korea
(Received 14 September 2005; published 25 January 2006)

A relativistic electron bunch with a large charge (>2 nC) was produced from a self-modulated laser wakefield acceleration configuration. For this experiment, an intense laser beam with a peak power of 2 TW and a duration of 700 fs was focused in a supersonic He gas jet, and relativistic high-energy electrons were observed from the strong laser-plasma interaction. By passing the electron bunch through a small pinholelike collimator, we could generate a quasimonoenergetic high-energy electron beam, in which electrons within a cone angle of 0.25 mrad ($f/70$) were selected. The beam clearly showed a narrow-energy-spread behavior with a central energy of 4.3 MeV and a charge of 200 pC. The acceleration gradient was estimated to be about 30 GeV/m. Particle-in-cell simulations were performed for comparison study and the result shows that both the experimental and simulation results are in good agreement and the electron trapping is initiated by the slow beat wave of the Raman backward wave and the incident laser pulse.

DOI: 10.1103/PhysRevE.73.016405 PACS number(s): 52.38.Kd

I. INTRODUCTION

There is a growing interest in generation of high-energy electron beams from plasma-based laser acceleration schemes [1,2]. In particular, electron trapping in the self-modulated laser wakefield acceleration (SMLWFA), in which the laser pulse is longer than the plasma period, $\tau \gg 2\pi\omega_p^{-1}$ [3–7], and the standard (resonant) laser wakefield acceleration, in which $\tau \approx 2\pi\omega_p^{-1}$ [8], have drawn great attention. In all of these schemes, some background plasma electrons are self-trapped and accelerated longitudinally by a relativistic plasma wave that is generated by the laser propagation in a plasma. In the past SMLWFA experiments [3–8], the generated electron energy spectra had the Maxwellian distribution, which means that most of the electrons are in the lower-energy range and a very small number of electrons are in the higher-energy range. Recently, a pronounced progress [9–11] has been made in electron beam generation from the LWFA; good-quality beams with a high charge, small emittance, and relatively small energy spread have been observed experimentally. The key for generating such a good-quality electron beam was the careful selection of the plasma and laser parameters such as the plasma density, laser pulse duration, acceleration length, and dephasing length (defined in Ref. [2]). Such femtosecond electron bunches could be useful in the pump-and-probe radiation chemistry [12] and in generating femtosecond intense x-ray pulses via Thomson or inverse Compton scattering [13] for probing ultafast phenomena in material science and biology.

As far as we know, however, the recent results [9–11] are not fully understood and cannot be repeated, strictly speaking, which means that we still do not have a reliable and controllable method for quasimonoenergetic beam generation. At the Center for Advanced Accelerators at Korea Electrotechnology Research Institute (KERI), we aim to find such methods to generate quasimonoenergetic electron beams. For this purpose, we used a pinholelike small collimator to select only high-energy electrons from the SMLWFA, where the high-energy electrons are separated from low-energy electrons due to different space-charge forces. Although this method has some limitations, it could be an intermediate way for better future methods. In our experiments, we used a very small collimator with a diameter of 1 mm and this method turned out to provide quasimonoenergetic electron beams with a few hundred pC in a reliable and repeatable way. In this paper, we report our experimental results from the pinholelike collimator method and the SMLWFA scheme. In Sec. II, the experimental setup is explained, and the measurements of the plasma density based on the Raman forward scattering method are described in Sec. III. Diagnostics of the quasimonoenergetic electron beams are described in Sec. IV, comparison of the experimental results with simulations is shown in Sec. V, and finally the conclusions are given in Sec. VI.

II. EXPERIMENTAL SETUP

The SMLWFA experimental setup is shown in Fig. 1. The experiment was carried out at KERI with a tabletop terawatt laser system that is based on the chirped pulse amplification technique [14]. Our laser system is a Ti:sapphire-Nd:glass hybrid type (built by Positive Light) and it produces p-polarized pulses of 700 fs in duration and 1.4 J in energy at the wavelength of 1.054 μm. Maximum peak power of the

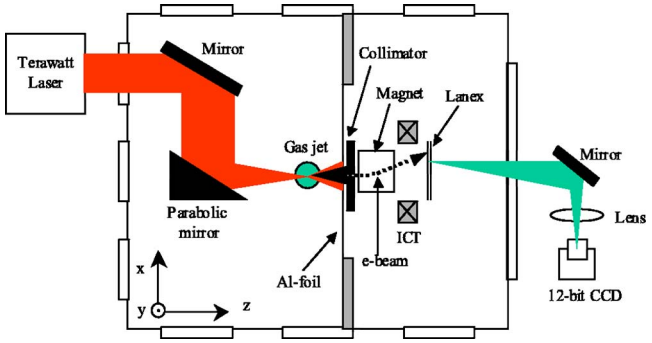

FIG. 1. (Color online) Schematic of the SM laser wakefield acceleration experiment at KERI.

laser pulse is 2 TW. The laser system consists of a Nd:glass oscillator, pulse stretcher, Ti:sapphire regenerative amplifier pumped by Nd:yttrium lithium fluoride laser beams, three-stage Nd:glass amplifiers pumped by flash lamps, and a pulse compressor. The laser pulse duration is measured by using a single shot autocorrelator. The pulse energy is monitored for every shot by using a calibrated fast photodiode. The laser beam is focused on the front edge of a supersonic helium gas jet by using a gold-coated off-axis parabolic mirror of $f/3$ focusing. The transverse beam pattern at focus is measured by imaging the focal plane onto an eight-bit charge-coupled device (CCD) camera coupled to an objective lens with a magnification factor of 60 (not shown in the figure). The focal spot size is calibrated with a tungsten wire of 50 μm thickness. The focal spot size in Fig. 2 is measured to be 10 μm (x direction)$\times$8 μm (y direction) in full width at half maximum (FWHM) with a Gaussian profile. So the maximum focal intensity is of the order of 1×10^{18} W/cm^2 and the Rayleigh length is $Z_R\approx176$ μm. The gas jet nozzle has a circular shape with an 800 μm orifice diameter and it is coupled to a commercial valve (General Valves) and mounted on an encoding three-dimensional translator to position the nozzle orifice relative to the laser focal spot precisely in vacuum. The helium gas is ejected into the vacuum in the interaction chamber where the pressure is maintained below 1×10^{-4} Torr. The backing pressure for the gas jet is within the range of 0–70 bars. The neutral gas distribution is measured [15] by using a Mach-Zehnder interferometer utilizing a separate neodymium-doped yttrium aluminum garnet (Nd:YAG) laser system. The density profile is Gaussian along the laser propagation (z) direction and exponentially decreasing in the vertical direction (y). Figure 3 shows the interference pattern and the fringe shift due to the He gas injection from the nozzle into the vacuum. Scattered light from the laser-plasma interactions are monitored with two eight-bit CCD cameras for top and side views to position the focal spot above the nozzle.

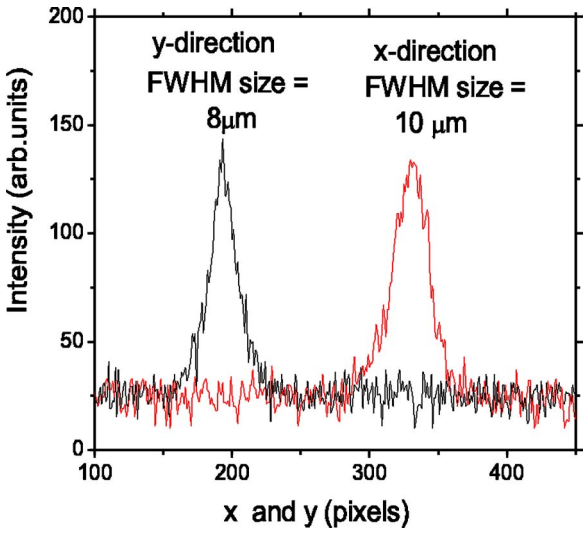

FIG. 2. (Color online) Laser focal spot transverse profiles in the x and y directions.

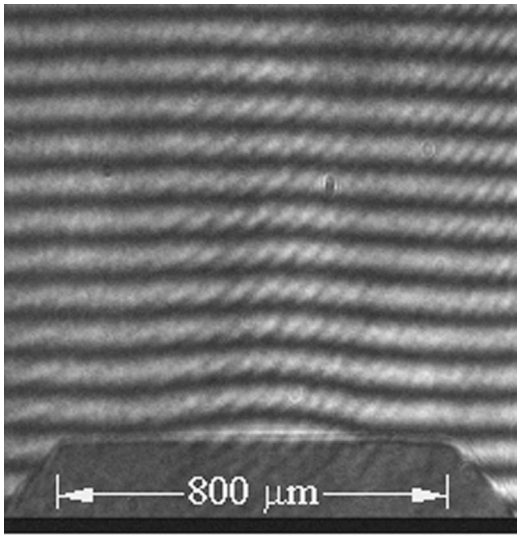

FIG. 3. Interference pattern of He gas ejected from the gas jet at backing pressure of 80 bars.

In order to measure the electron energy, energy spread, and charge, we used several tools. First, a quasimonoenergetic electron beam is generated with a stainless steel collimator allowing on-axis electrons within a cone of $f/70$ to propagate through it. Then, a permanent dipole magnet (with dimensions of 10 mm in gap distance, 25 mm in length, and 40 mm in width, and a magnetic field strength of 0.3 T) for energy and energy spread measurement is used. A fluorescence screen Lanex (Kodak Fast Screen) and a high-resolution 12-bit CCD camera are used to monitor the electron beam profile. By comparing the undispersed beam image (for $B=0$) with the dispersed one, the electron beam energy is calculated by using an electron trajectory code. In addition, the charge per bunch is measured by an integrating current transformer–beam (ICTBCM) charge monitor made by Bergoz Instruments. Measurement of the forward Raman scattering is also performed by focusing a small portion of the transmitted laser light (after interacting with the plasma) into an optical spectrometer (HR-2000, Ocean Optics) and the electron beam signal is simultaneously monitored by the ICTBCM.

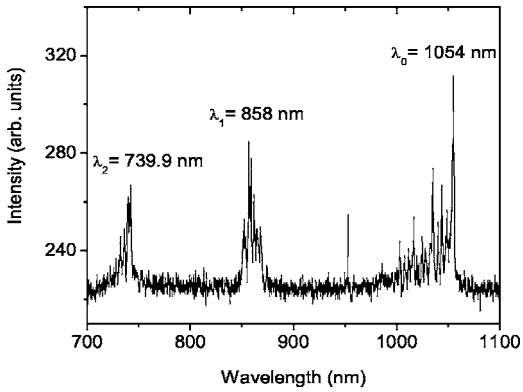

FIG. 4. Spectrum of the Raman forward scattered light showing the first and second anti-Stokes sidebands.

III. DETECTION OF RAMAN FORWARD SCATTERING AND MEASUREMENT OF PLASMA ELECTRON DENSITIES

Raman (forward and backward) scatterings are interesting fundamental phenomena in intense laser-plasma interactions [16–18]. In the Raman forward scattering (RFS), an electromagnetic wave (ω_0, k_0) incident upon a plasma scatters into two copropagating electromagnetic sidebands $(\omega_0 \pm \omega_p, k_0 \pm k_p)$ and a plasma wave (ω_p, k_p). For large amplitude plasma waves, nonlinear steepening results in harmonics in the frequency $\omega_0 \pm n\omega_p$. The RFS has the potential to generate relativistic electrons because the resulting plasma wave (ω_p, k_p) has a relativistic phase velocity nearly equal to the speed of light c. Here $\omega_p = (4\pi n_e e^2/\gamma m_0)^{1/2}$ is the plasma frequency, where $\gamma = (1+a^2)^{1/2}$ is the relativistic factor associated with the electron motion perpendicular to the laser propagation direction and $a = eE/m_0\omega_0 c$ is the laser's normalized vector potential. So detection of RFS is evidence for the plasma wave existence and at the same time it is a direct online method for measuring the plasma electron density n_e from the amount of frequency shift between the laser light and the sidebands. In our experiment, the RFS spectrum showed that the first and second anti-Stokes sidebands are located at $\lambda_1 = 858$ nm and $\lambda_2 = 739.9$ nm, respectively, in the transmitted laser light as shown in Fig. 4. Simultaneously with the RFS observation, the electron beam signal was monitored by the ICT. When the laser beam power was reduced to the level of 10^{15} W/cm^2, the RFS and the signal from the beam charge monitor were not observed. Only at relatively high power, 1.5 TW in this case, did we observe both signals. By changing the backing gas pressures, we observed changing of the Raman shift of the first anti-Stokes signal, as shown in Fig. 5. The dashed line in Fig. 5 shows the location of the laser line $\lambda_0 = 1.054$ μm and the arrows show the location of the first anti-Stokes Raman sideband. The plasma density was inferred from the Raman shift at various gas jet backing pressures up to 60 bars. The relation of the density versus backing pressure was obtained in the pressure range of 30–60 bars and the result is shown in Fig. 6, which indicates that the plasma density is in the range of $2.8 \times 10^{19} - 4.5 \times 10^{19}$ cm^{-3}. The plasma wavelength λ_p (μm) $= 3.3 \times 10^{10} n_e^{-1/2}$ (cm^{-3}) is also plotted in the same figure. Modulation (and hence the nomenclature of SMLWFA) of the laser pulse was also observed and it was increasing with the plasma density.

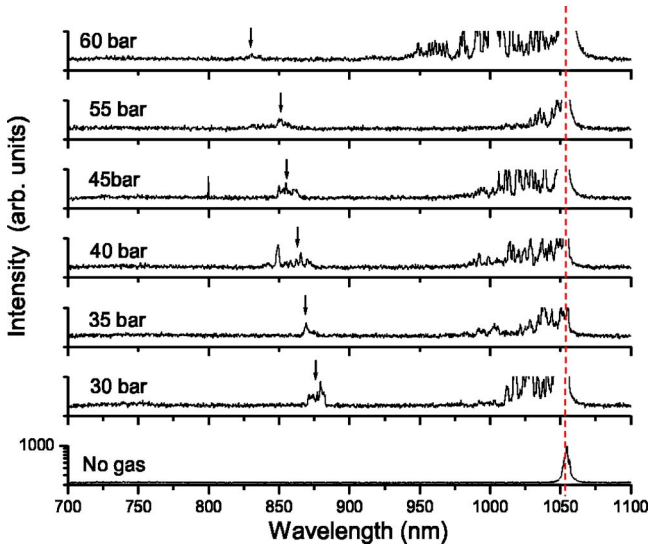

FIG. 5. (Color online) Spectrum of the Raman forward scattered light for various helium gas jet backing pressures. Here 1.5 TW laser power was used.

IV. ELECTRON BEAM DIAGNOSTICS

The electron beam emitted from the laser-plasma interaction was first monitored by observing a strong light emitted from the Lanex film after the beam passed through it. In order to make sure that the signal was truly due to the electron beam, not due to x rays, an electromagnet was used in the beginning and the light from the Lanex film was confirmed to come from the electron beam. The total beam charge was monitored by the ICTBCM set. Typical wave forms of beam charge monitoring from the ICTBCM are shown in Fig. 7. The ICT was installed along the beam path

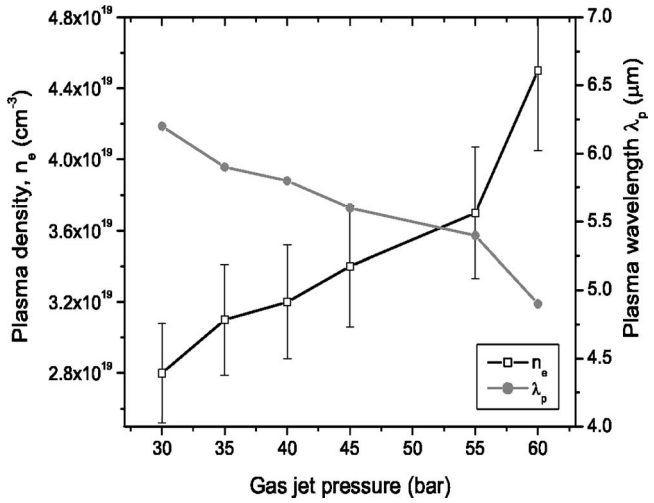

FIG. 6. Measured plasma densities and plasma wavelengths based on the Raman forward scattered light in Fig. 5.

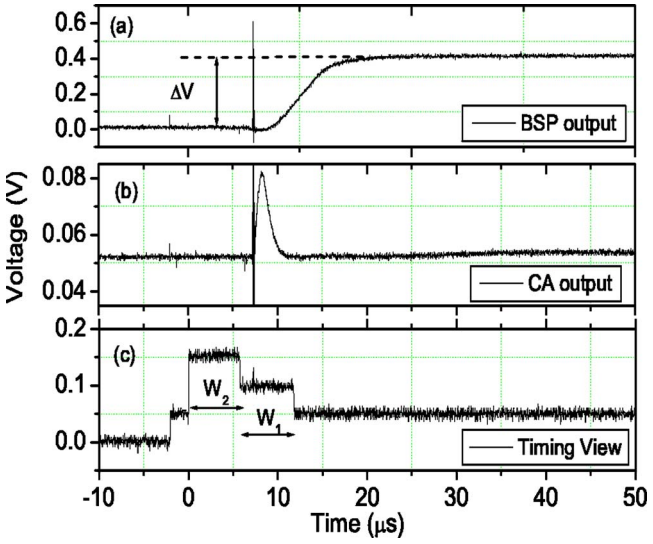

FIG. 7. (Color online) Typical wave forms of the beam charge monitoring system (ICTBCM unit). BSP and CA stand for bunch signal processor and charge amplifier, respectively.

at a distance of 50 mm past the gas jet. When an electron bunch passes through the ICT, a fast (20 ns rise time) electrical signal is produced and is sent to the BCM unit for processing. The timing view shown in Fig. 7(c) helps in adjusting the time delay for triggering the BCM unit, so that the beam pulse falls within the integration window (the subtracting window W_1 in this case). Inside the BCM unit, the charge amplifier amplifies the signal, which is shown in Fig. 7(b). Then the signal goes to the bunch signal processor, a core part of the BCM unit. When the BCM is externally triggered, the BSP integrates the signal and produces the final output pulse that is shown in Fig. 7(a). The voltage difference ΔV=400 mV of Fig. 7(a) corresponds to a beam charge of 2 nC. Such a large charge was also produced in similar experiments with different beam charge monitoring techniques [6,7].

The beam profile was measured on the Lanex screen at various locations from the gas jet. We found the beam size is rather large ($\sim$1 cm), which means that the beam diverges very rapidly as it propagates in vacuum. This is an expected behavior because the electron beam coming out of the plasma has a very large charge ($\sim$1 nC) per pulse, a very small beam size (λ_p), and a very short duration ($\sim$ laser pulse duration). A simple calculation shows that the space charge force is enormous and the electron beam expands almost explosively as it propagates. In our measurement, the FWHM of the beam's transverse profile was 50 mm at a distance of 70 mm from the gas jet, so the beam divergence cone angle is 0.68 rad or 39°. Here, it should be noted that high-energy electrons are concentrated on the axis with a high density, while low-energy electrons are distributed around the high-energy electrons with a lower density due to the space-charge effect. Hence, a collimator with a pinholelike aperture of 1 mm diameter was installed along the axis of the beam propagation direction to select only high-energy electrons. In this way, high-energy electrons within a collection cone of $f/70$ were selected and allowed to propagate in free space. The charge of this beam was measured to be about 200 pC per bunch, which is large enough for many applications. The beam also showed that it expands very rapidly in the free space due to a strong space-charge force.

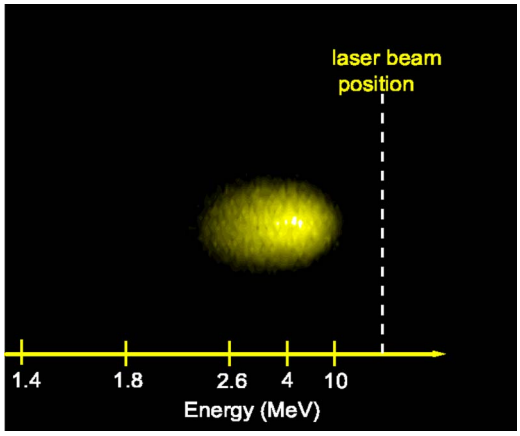

FIG. 8. (Color online) Energy spectrum of the electron beam measured by a dipole magnet (B-field intensity = 0.3 T); the beam is clearly quasimonoenergetic with energy of 4.3±2 MeV.

Energy spectrum of the beam was obtained by using the Lanex film and the dipole magnet coupled with the 1 mm collimator. At 1.5 TW laser power and 2.8×10^{19} cm^{-3} plasma density, the electron beam image profile is shown in Fig. 8, which indicates that the beam has a narrow energy spread $\sim\pm2$ MeV and the central energy is about 4.3 MeV. This energy spectrum is different from the typical one coming from self-modulated laser wakefield accelerators. When a larger diameter collimator was used (for example, 5 mm in diameter as reported in earlier experiments [5–7]), the beam energy behaves as a Maxwellian distribution. Hence, the experimental result clearly shows that the pinholelike small collimator method works toward the generation of quasimonoenergetic beams from the SMLWFA. In our experiment, the diffraction length is $2Z_R\sim350$ μm, so the maximum acceleration gradient is approximately 30 GV/m.

The behavior of electron beam energy and charge versus the plasma density was also measured and the result is shown in Fig. 9. A noticeable feature in this graph is that the beam energy starts low at low density and then increases with density and drops at higher plasma density. This experimental result can be explained qualitatively as follows. At a lower density the acceleration gradient is lower, so the beam energy is relatively low. As the plasma density increases the acceleration gradient increases and the beam energy also increases. At increased higher density the beam experiences dephasing and it eventually reaches a deceleration phase of the wave, so the energy drops. Although the beam energy changes with a density, it preserved the quasimonoenergetic characteristics within the plasma density range shown in Fig. 9.

V. SIMULATION RESULTS

We carried out one-dimensional particle-in-cell (PIC) simulations of the self-modulation laser wakefield accelera-

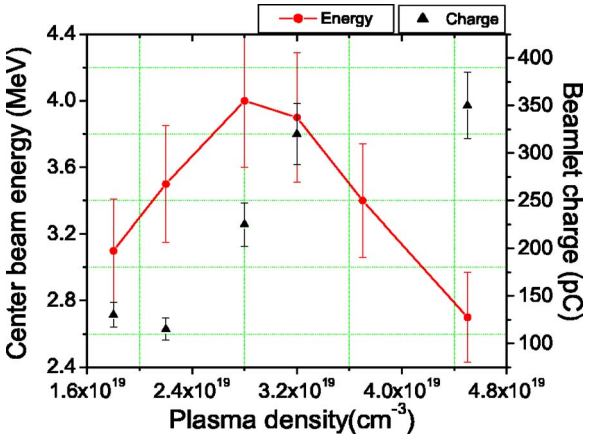

FIG. 9. (Color online) Behavior of the central energy and charge of the electron beam as a function of plasma density.

tion [19]. For these simulations, the one-dimensional version of XOOPIC [20] was used with laser parameters the same as in the experiment: the laser intensity was 2.7×10^{18} W/cm^2, corresponding to the normalized vector potential $a=eA/mc^2=1$, and the pulse duration was 700 fs (FWHM). Infinitely long and uniform plasmas were used with plasma densities of $n_p=1.95\times10^{19}$, 2.35×10^{19}, 3.01×10^{19}, and 4.01×10^{19} cm^{-3}, respectively.

Figure 10 shows the evolution of the laser pulse and its spatial spectrum for $n_p=1.95\times10^{19}$ cm^{-3}. The spectrum of the laser pulse at $t=2.0$ ps exhibits anti-Stokes signals up to the third order. Those high-frequency anti-Stokes signals are the results of the interaction between the incident laser field and the higher-harmonic components of the plasma wave originating from its nonlinear steepening. Up to the second anti-Stokes signal was measured in our experiment (Fig. 4). A similar spectral feature measured from experiment can also be found in [7].

The modulated laser pulse in Fig. 10(b) resonantly drives the wakefield in the plasma in the longitudinal direction, which is presented in Fig. 11 along with the corresponding electron phase space captured at $t=2.0$ ps. The zoomed-in figure [see Fig. 11(a), inset] shows a steepening of the

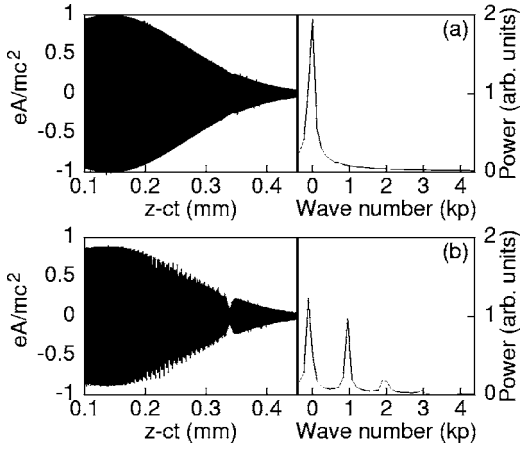

FIG. 10. Snapshots of the driving laser pulse and its power spectrum at $t=$ (a) 0.7 and (b) 2.0 ps.

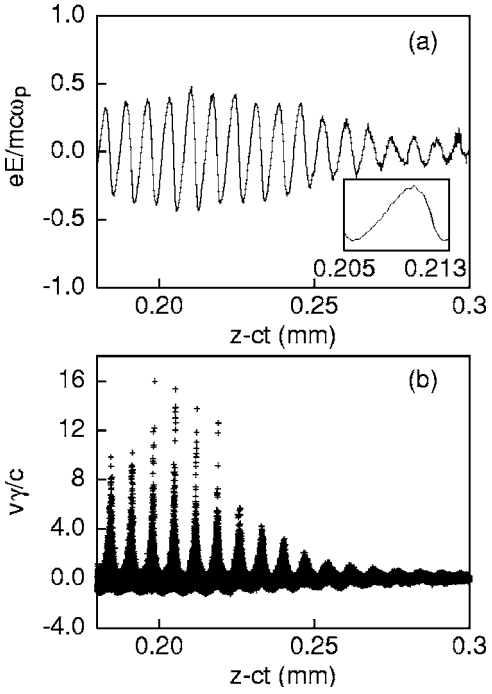

FIG. 11. (a) Plasma wave (wakefield) and (b) electron phase space at $t=2.0$ ps.

plasma wave. The wave breaking limit in the relativistic regime is determined by $eE_{WB}/mc\omega_p=\sqrt{2(\gamma_p-1)}$, where $\gamma_p=1/\sqrt{1-v_p^2/c^2}$ and v_p is the phase velocity of the plasma wave [21]. For the plasma density $n_p=1.95\times10^{19}$ cm^{-3}, $\gamma_p\simeq\omega/\omega_p=7.6$, which leads to the wave breaking limit $eE_{WB}/mc\omega_p=3.6$. The accelerating electric field in Fig. 11 shows much less amplitude than the required value for wave breaking, which strongly implies that the electron trapping in the simulation was initiated by the slow beat wave of the Raman backscattered wave and the original pulse [7,22]. The linear growth rate of the Raman backscattering (RBS) is, from [23], $\gamma_{RBS}=a\sqrt{\omega\omega_p}/4$, which is 1.7×10^{14} for the laser and plasma parameters used in Figs. 10 and 11. Thus, the normalized vector potential of the backscattered signal at $t=1.8$ ps, where the trapping begins, should be a result of more than hundreds of e-foldings. To confirm this, we separately measured in the simulations the right-going signal (the original signal and various Stokes and anti-Stokes signals), and the left-going one (backscattered wave), by $E_{left}=0.5(E_y-cB_z)$ and $E_{right}=0.5(E_y+cB_z)$ [24] (the electric field is assumed to be propagating in the x direction and polarized in the y direction). We found that the amplitude of the backscattered wave typically reaches more than 10% of the original laser pulse amplitude. The normalized plasma wave $eE/m\omega_pc$ is measured to be around 0.5 in Fig. 11. Those values satisfy the threshold condition for electron trapping by colliding laser beams [22].

Figure 12(a) shows the electron beam energies as a function of distance, obtained from the simulations. The collimator, which picks up the monoenergetic portion of the electron beam in the experiment, could not be incorporated self-consistently in the one-dimensional simulations. Instead, we averaged the energy of the trapped electrons with a cutoff at

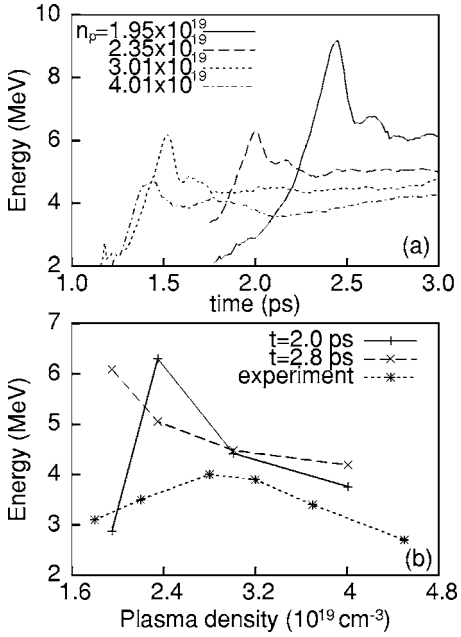

FIG. 12. Measurements of averaged energy of trapped electrons as functions of time (a) and comparison with the experimental results (b).

2 MeV. For given laser parameters, the energy of the electron beams accelerated by the wakefields is governed by the plasma density via the growth length of the Raman forward scattering and the dephasing length: RFS grows faster for higher electron density evoking earlier excitation of the wakefield, but the electrons reach more quickly the dephasing limit. The growth rate of the electron energy is roughly proportional to the Raman growth in the forward direction, which scales as ω_p^2. The dephasing time [2] $L_{\mathrm{dp}}/c = (\omega_0^2/c\omega_p^2)\lambda_p$ scales as ω_p^3. These rough scaling laws were verified from the simulation data. The dephasing time is determined from Fig. 12(a) by measuring the time interval between the beginning of energy ramping up and the starting of the saturation. The energy growth rate for each density could be obtained simply by measuring the slope of the left tails in Fig. 12(a). Fitting those measures by a trial function $\beta\omega_p^\alpha$ resulted in $\alpha \simeq 2.1$ for the energy growth, and $\alpha \simeq 3.5$ for the dephasing time, which confirms the scaling law. Because the dephasing is more strongly dependent on ω_p than the energy growth, the saturation level of the beam energy shows a monotonically decreasing curve as a function of the density (or ω_p). Another remark should be made. Even though the saturation level of the beam energy is monotonically decreasing as a function of density, the convex shape of the energy-density profile in Fig. 9 still can be obtained by using a plasma shorter than the saturation length. For example, if the energy is measured at $t \simeq 2.0$ ps in Fig. 12(a), which corresponds to a plasma of 0.6 mm in the longitudinal direction, the beam energy (as a function of density) behaves in a similar manner as in the experiment (Fig. 9). This argument is compatible with our experimental condition: the hole size in the gas jet was 0.8 mm and the region of flat density must have been much shorter due to the gas diverging near the edge (see Fig. 3). A direct comparison of the beam energies from experiment and simulation was made at different times (which corresponds to the plasma size) as shown in Fig. 12(b).

VI. CONCLUSIONS

The experimental results, supported by one-dimensional PIC simulation, demonstrated that the pinholelike small collimator method can produce narrow-energy-spread electron beams from SMLWFA that originally produces electrons with a continuous energy distribution. In this method, only high-energy electrons on the propagation axis were selected to pass through the small collimator and the measured energy spectrum clearly showed quasimonoenergetic characteristics. The charge per pulse is large enough ($Q \sim$ a few hundred pC) for many applications (radiation chemistry, for example) as high-energy electrons around the axis have a much higher density than low-energy electrons. Furthermore, the energy spectrum and the charge of the electron beam bunch can be easily controlled by using collimators with different pinhole sizes. Therefore, the pinholelike small collimator method is very simple, but it could be a very useful and practical way for good-quality beam generation.

ACKNOWLEDGMENTS

We thank V. Malka, J. Faure at LOA, J. Bergoz at Bergoz Instruments, and J. Wurtele at UC Berkeley for helpful discussions. This research was supported by the Korean Ministry of Science and Technology through the Creative Research Initiative (CRI) Program.

[1] T. Tajima and J. M. Dawson, Phys. Rev. Lett. **43**, 267 (1979).
[2] E. Esarey *et al.*, IEEE Trans. Plasma Sci. **24**, 252 (1996), and references therein.
[3] K. Nakajima *et al.*, Phys. Rev. Lett. **74**, 4428 (1995).
[4] A. Modena *et al.*, Nature (London) **377**, 606 (1995).
[5] C. A. Coverdale *et al.*, Phys. Rev. Lett. **74**, 4659 (1995).
[6] D. Umstadter *et al.*, Science **273**, 472 (1996).
[7] C. Moore *et al.*, Phys. Rev. Lett. **79**, 3909 (1997).
[8] V. Malka *et al.*, Science **298**, 1596 (2002).
[9] S. P. Mangles *et al.*, Nature (London) **431**, 535 (2004).
[10] C. G. Geddes *et al.*, Nature (London) **431**, 538 (2004).
[11] J. Faure *et al.*, Nature (London) **431**, 541 (2004).
[12] A. Ogata *et al.*, IEEE Trans. Plasma Sci. **24**, 453 (1996).
[13] N. Hafz *et al.*, J. Korean Phys. Soc. **44**, 1274 (2004).
[14] M. Perry and G. Mourou, Science **264**, 917 (1994).
[15] Changbum Kim, Ph.D. dissertation, Pohang University of Science and Technology, Pohang, Korea, 2005 (unpublished).
[16] W. B. Mori *et al.*, Phys. Rev. Lett. **72**, 1482 (1994).

[17] E. Esarey *et al.*, Phys. Rev. Lett. **72**, 2887 (1994).
[18] M. S. Hur *et al.*, Phys. Rev. Lett. **95**, 115003 (2005).
[19] Full scale two-dimensional PIC simulation of SMLWFA employing a long laser pulse (τ=700 fs$\gg 2\pi/\omega_0$) is planned in the near future.
[20] H. Usui *et al.*, IEICE Trans. Electron. **E83C**, 989 (2000).
[21] A. I. Akhiezer and R. V. Polovin, Sov. Phys. JETP **3**, 696 (1956).
[22] C. B. Schroeder *et al.*, Phys. Rev. E **59**, 6037 (1999).
[23] W. L. Kruer, *The Physics of Laser Plasma Interactions*, Frontiers in Physics (Addison-Wesley, Reading, MA, 1988).
[24] P. Mardahl *et al.*, Phys. Lett. A **296**, 109 (2002).